Applied Geochemistry 47 (2014) 130–140

Contents lists available at ScienceDirect

Applied Geochemistry

journal homepage: www.elsevier.com/locate/apgeochem

Redox reaction of aqueous selenite with As-rich pyrite from Jiguanshan ore mine (China): Reaction products and pathway

Mingliang Kang [a,b,e], Fabrizio Bardelli [b], Laurent Charlet [b,*], Antoine Géhin [b], Andrey Shchukarev [c], Fanrong Chen [a], Marie-Christine Morel [d], Bin Ma [e], Chunli Liu [e]

[a] CAS Key Laboratory of Mineralogy and Metallogeny, Guangzhou Institute of Geochemistry, Chinese Academy of Sciences, Guangzhou 510640, China
[b] Environmental Geochemistry Group, ISTerre, University of Grenoble I, 38041 Grenoble, France
[c] Department of Chemistry, Umeå University, Umeå SE-901 87, Sweden
[d] Laboratoire d'Etude des Transferts en Hydrologie et Environnement, University of Grenoble I, 38041 Grenoble, France
[e] Fundamental Science Laboratory on Radiochemistry & Radiation Chemistry, College of Chemistry and Molecular Engineering, Peking University, Beijing 100871, China

ARTICLE INFO

Article history:
Available online 12 June 2014
Editorial handling by M. Kersten

ABSTRACT

The interaction of an As-rich natural pyrite ($FeS_{2.08}As_{0.043}$) with aqueous Se(IV) was investigated as a function of pH, ferrous iron concentration, and reaction time. Arsenic is often the most abundant minor constituent of natural pyrite, and is believed to substitute for S in the pyrite structure. EXAFS measurements confirmed the presence of AsS dianion group, with arsenic in the same local configuration as in the arsenopyrite. Speciation studies indicated that Se(0) was the unique reduction product in the pH range 5.05–8.65 over a reaction period of >1 month, while trace amounts of $FeSeO_3$ might be formed at pH $\geqslant$ 6.10. At pH > 6.07, the formation of Fe(III)-(oxyhydr)oxide is kinetically favored, and it consumed nearly all the aqueous iron, including the extra added Fe^{2+}, thereby inhibiting the formation of the thermodynamically most stable product: $FeSe_2$. After oxidation by Se(IV), the occurrence of surface S^0, significant aqueous sulfur deficit, and excessive leaching of arsenic in solution, indicate the preferential release of As impurity via arsenopyrite oxidation. The data suggest that the polysulfide-elemental sulfur pathway, which prevails in acid-soluble metal sulfides, is an important pathway in the oxidation of As-rich pyrite, in addition to the thiosulfate pathway for acid-insoluble pyrite. Control experiments on As-free natural pyrite further support this mechanism. This study confirms the potential of reductive precipitation to attenuate the mobility of Se in the environment and demonstrates that minor elements commonly present in natural pyrite can play a significant role on its dissolution pathway.

1. Introduction

Selenium is essential to human life and diseases related to both its excess and deficiency occur all over the world (Fordyce et al., 2000; Klaasen, 2008; Rayman, 2008). In addition, the radioactive isotope ^{79}Se, with a half-life of 3.77×10^5 years (Bienvenu et al., 2007), is presently considered as a key mobile fission product for the disposal of spent fuel and high-level radioactive waste (Chen et al., 1999; Grambow, 2008). For these reasons, Se mobility and bioavailability is of major interest in soil and environmental sciences, and an important concern for the safe disposal of radioactive waste.

The solubility of selenium is significantly controlled by its oxidation state, which in turn depends on the redox conditions of the surrounding environment. Tetravalent and hexavalent Se are much more soluble and mobile aqueous oxyanions than zero or lower oxidation states Se species (Scheinost and Charlet, 2008; Scheinost et al., 2008). Due to the limitations in physisorption of Se(IV) and Se(VI) on natural minerals (the sorption efficiency is relatively low and the sorption reaches saturation soon), in particular on granite and claystone minerals that are considered as host rock candidates for nuclear waste disposals (Baryosef and Meek, 1987; Guo et al., 2011), reductive precipitation is expected to be the most effective way to immobilize ^{79}Se.

On the other hand, pyrite (FeS_2) is the most widely distributed metal sulfide mineral in the geological environment, and is also present in claystones and granitic rocks (Baeyens et al., 1985; Metz et al., 2003; Gaucher et al., 2004). Owing to its strong reducing ability, and to its stability under anoxic conditions, pyrite is expected to be one of the major reductive components in candidates host rocks for radioactive waste disposal, and, therefore, to give an important contribution to limit the release of redox-sensitive radionuclides like ^{79}Se on a geological time-scale.

* Corresponding author. Tel.: +33 (0) 476 63 5198; fax: +33 (0) 476 63 5252.
E-mail address: charlet38@gmail.com (L. Charlet).

http://dx.doi.org/10.1016/j.apgeochem.2014.05.018
0883-2927/

Selenium speciation on pyrite surfaces has been the subject of many studies, but conflicting results have been reported. For example, Breynaert et al. (2008) found crystalline Se(0) as the only Se-bearing reaction product of the pyrite-Se(IV) reaction between pH 6.5 and 8.5. Elemental Se was also observed as the reaction product of pyrite-HSe^- reaction at pH 6.6 (Liu et al., 2008), and Se(IV)-doped pyrite at pH values ranging from 3.7 to 5.0 (Diener et al., 2012). On the other hand, Naveau et al. (2007) excluded the formation of Se(0) and suggested either Se(-I), or Se(-II) solids were formed when aqueous Se(IV) and Se(-II) reacted with pyrite at pH 3.0. The different results observed in the above experiments suggest that Se speciation on pyrite surface is significantly affected by the physico-chemical condition under which the reactions occur. Thermodynamically, in nearly neutral to alkaline conditions, $FeSe_2$ should be the predominant product in pyrite-containing systems, and ferrous iron can favor its formation (Charlet et al., 2012).

The kinetics and mechanism of pyrite oxidation are of great concern in geochemistry and environmental science research, because of its main role in acid mine drainage (AMD) (Moses and Herman, 1991; Williamson and Rimstidt, 1994; Descostes et al., 2004). In addition to sulfate, elemental sulfur was also observed as an endproduct of pyrite oxidation (Sasaki et al., 1995). Luther (1997) proposed that the decomposition of sulfur intermediates (e.g., thiosulfate) could lead to these endproducts and the nonstoichiometric dissolution of pyrite. However, the influence factors on the pyrite oxidation pathway are still not well-documented.

Naturally occurring pyrite commonly contains minor substituted metals and metalloids (As, Se, Hg, Cu, Ni, etc.). Arsenian pyrites, for example, may contain up to 10% As (Rimstidt and Vaughan, 2003). Nevertheless, the studies linked to the influence of these minor or trace elements on pyrite oxidation are very few.

In this study, redox reaction between natural As-rich pyrite and aqueous Se(IV) were conducted in the pH range 5.05–8.65. The effects of adding ferrous ion and of the reaction time on the reduction products, as well as the effect of arsenic impurity on pyrite dissolution pathway, were investigated. The results were interpreted in light of thermodynamic calculations, X-ray Absorption Spectroscopy (XAS), X-ray Photoelectron Spectroscopy (XPS), and solution analyses.

2. Materials and methods

2.1. Chemicals

Arsenic-rich pyrite from the Jiguanshan ore mine (Tongling, China), hereafter called As-rich pyrite, was used in this study. Large pyrite crystals were crushed, and the particle fraction 90–120 μm in size was selected by sieving. Magnetic separation was employed to remove pyrrhotite and iron oxide impurities. Then pyrite was ultrasonically washed using degassed water, 0.2 M HCl, ethanol and acetone, and finally dried and stored in a glove box in nitrogen atmosphere (O_2 < 2 ppm). Before introduction in the reaction solution, the pretreated pyrite grains were further ground to a fine powder in the glove box using an agate mortar. The specific surface area of the ground pyrite powder was measured to be $0.48 \pm 0.05\ m^2\ g^{-1}$ by BET N_2-absorption method. X-ray diffraction (XRD) and Mössbauer analyses only detected pyrite (Figs. A.1 and A.2), indicating that minor phases, if present, are below the detection limit of these techniques (~5% of the prevalent phase for XRD). The stoichiometric ratio (S/Fe) of the sample, measured by SEM-EDS (Scanning Electron Microscopy – Energy Dispersive Spectroscopy), was equal to 2.08. Natural pyrite typically contains a host of minor and trace elements. Inductively Coupled Plasma-Optical Emission Spectroscopy (ICP-OES) analysis, after aqua regia dissolution of the sample, showed that this natural pyrite contains 2.56 wt% arsenic (i.e. $FeS_{2.08}$–$As_{0.043}$), while no other elements (B, Co, Cu, Ni, Pb, Si) were detected using this technique.

Commercially available arsenic-free natural pyrite ($0.19 \pm 0.02\ m^2\ g^{-1}$) used for control experiments, and hereafter called As-free pyrite, was purchased from Alfa Aesar. SEM-EDS analysis performed on this sample indicated an average S/Fe ratio of 2.07. ICP-OES analysis after aqua regia dissolution showed that the sample contained ~0.44 wt% Co (i.e., $FeS_{2.07}Co_{0.0089}$), while As, Ni, Cu, and Zn were absent or under detection limit.

All other chemicals used in this study were of analytical grade. The water used was deionized (18.2 MΩ cm) and boiled purging with argon before introduction in the glove box. Seven references were used as XAS standards: amorphous red Se(0) was synthesized via chemical reduction of Na_2SeO_3 by glutathione following the procedure mentioned in Huang et al. (2003), while $FeSe_2$ was synthesized according to the protocol mentioned by Liu et al. (2006). Commercial Na_2SeO_4 (MERCK), $Na_2SeO_3{\cdot}5H_2O$ (Sigma Aldrich), crystalline grey Se(0) (Sigma Aldrich), and FeSe (Alfa Aesar) were used as Se(VI), Se(IV), Se(0), and Se(-II) references, respectively. $FeSeO_3$ reference was the same used in a previous work (Kang et al., 2011).

2.2. Redox reaction experiments

Redox reactions were conducted in two series of experiments. In the first one, experiments were performed in continuously stirred batch reactors sealed and kept in O_2-free (O_2 < 2 ppm) glove box at pH 5.05, 5.65, and 6.10. In each reactor, 10.5 g of As-rich pyrite powder was equilibrated for 4 days with 1000 mL of 0.01 M NaCl solution before adding 4.2, 4.6, and 5.0 mL of 0.1 M Na_2SeO_3 solution, respectively. A buffer solution of CH_3COONa–CH_3COOH (~0.05 M) was used to adjust the pH to the desired values. To further elucidate the effect of arsenic impurity on pyrite dissolution pathway, control experiments on the As-free pyrite (8.0 g/L) were performed at pH 4.26 and 4.50 with an initial selenite concentration of 0.4 mM.

In the second series of experiments, 0.4 mM of Se(IV) was added to 5.5 g/L As-rich pyrite suspension, which was previously equilibrated in a 0.02 M NaCl ionic background solution in a 250 mL reactor for 2 days. The experiments were performed in four reactors, with initial pH of 6.94, 8.65, 6.07 and 7.51, respectively. No buffer solution was used for the reactions at pH 6.94, 8.65, and 7.51, while at pH 6.07 ~0.05 M CH_3COONa–CH_3COOH buffer solution was used. To investigate the effect of Fe^{2+} on the Se(IV) reduction product, 0.10 and 0.08 mM $FeCl_2$ were initially added to the reactions at pH 6.07 and 7.51, respectively. The reactors were manually shaken several times each day. During the reaction process, the solution pH in all reactors was left free to vary. At defined time intervals, the solution pH was measured with a Metrohm 6.0233.100 pH electrode connected to an Orion (525A) pH meter. Redox potentials were measured using a WTW Sentix ORP Pt combination electrode with Ag/AgCl reference. The electrode was calibrated using a commercial Mettler–Toledo redox buffer (220 mV at 25 °C). Meanwhile, an aliquot of 6 mL suspension from each reactor was sampled and filtered using 0.2 μm pore size membranes (Millipore). Total Fe, S, Se, and As concentrations in the filtrate were analyzed by ICP-OES (Varian 720-ES), with detection limits of 8.95×10^{-8}, 5.21×10^{-7}, 3.80×10^{-7}, and 1.33×10^{-7} mol/L, respectively. The Fe^{2+}/Fe^{3+} ratio was determined by the phenanthroline method, with and without a reduction step by hydroxylamines (Viollier et al., 2000). Solution results are shown in Tables B.1–B.3.

The elemental sulfur formed on the As-rich pyrite surface after oxidation by Se(IV) was quantitatively measured by extraction in perchloroethylene and subsequent quantitative analysis by

high-performance liquid chromatography (HPLC), following the method developed by McGuire and Hamers (2000). These results are shown in Table B.4.

2.3. X-ray absorption spectroscopy

Aliquots of As-rich pyrite suspensions (15 mL) were sampled after 7, 21, and 34 days of reaction from the first series of experiments, and 44 days of reaction from the second series of experiments. These suspensions were filtered with 0.2 μm porous membranes (Millipore). The filtered powder was dried with silica gel, sealed with Kapton tape, and mounted on the sample holder. All the above manipulations were conducted inside a glove box with N_2 atmosphere (O_2 < 2 ppm). The samples were then brought to the synchrotron facility in an anaerobic jar and quickly transferred in the experimental vacuum chamber (10^{-6} mbar).

XAS measurements were performed at the Se and As K-edges (12,658 and 11,867 eV, respectively) on the Italian beamline (BM8-GILDA) at the European Synchrotron Radiation Facility (ESRF) in Grenoble (France). In order to avoid beam-induced redox reactions and to enhance the EXAFS signal at high *k*, all samples and reference standards were measured in vacuum and at low temperature (77 K), using a nitrogen cryostat. A Se(0) reference was simultaneously acquired at each energy scan for accurate energy calibration. The fluorescence signal from the samples was acquired using a 13-element Ge detector, suitable for detection of diluted elements. To optimize the fluorescence signal from the samples the geometry described in Maurizio et al. (2009) was used. Detailed information on XAS experimental setup and data analysis is reported in Appendix C.

Principle Component Analysis (PCA) and Least Square Fitting (LSF) were applied to the XANES spectra to obtain quantitative information on samples' speciation (Ressler et al., 2000). PCA and LSF were performed using the SIXPACK and IFEFFIT packages, respectively (Ravel and Newville, 2005; Webb, 2005). Local structure around Se was obtained by quantitative refinements of the EXAFS signal up to the third coordination shell (~3.5 Å), when present. Fits were performed in the back-transformed reciprocal space (k = 4–12 Å^{-1}) using a dedicated software package (Meneghini et al., 2012; Monesi et al., 2005) based on MINUIT routines from CERN libraries (James and Roos, 1975). The ATOMS (Ravel, 2001) software was used to generate the atomic clusters centered on the absorber atom, which were used as starting structures to calculate the EXAFS theoretical amplitude and phase back-scattering functions using the FEFF8 code (Ankudinov et al., 1998).

2.4. X-ray photoelectron spectroscopy

XPS measurements were performed on samples reacted for 220 days from the first series of experiments, and on samples reacted for 70 days from the second series of experiments. To avoid possible oxidation, all samples were dried in the glove box with silica gel, sealed in glass bottles, and brought to Umeå University (Sweden) in an anaerobic jar for XPS analyses. A wet $Fe(OH)_2$ reference was prepared in the same way and showed no oxidation. Before measurements, samples were pressed into pellets in Argon atmosphere and immediately transferred to the XPS vacuum chamber. XPS spectra were recorded with Kratos Axis Ultra electron spectrometer equipped with a delay line detector. The monochromated Al K_α source operated at 150 W. A hybrid magnetic lens system and a charge neutralizer provided an analysis area of 0.3 × 0.7 mm. The binding energy (BE) scale was referenced to the C 1s line of aliphatic carbon (285.0 eV). Processing of the spectra was accomplished using the Kratos software.

3. Results and discussion

3.1. X-ray absorption spectroscopy

As K-edge: It is generally accepted that, in pyrite, arsenic substitutes for sulfur forming either AsS or AsAs dianion groups (Foster et al., 1998; Simon et al., 1999; Savage et al., 2000). Based on DFT calculations on pyrite with a comparable amount of As impurity (~1.9%), Blanchard et al. suggested that the substitution of S_2 units by AsS groups is energetically favored compared to that of As_2 groups, and proposed a model in which As substitutes in the pyrite structure in a local configuration very close to that of arsenopyrite (Blanchard et al., 2007).

Arsenic K-edge absorption spectroscopy was used to shed light on As local environment in our As-rich pyrite sample. The absorption spectrum of our sample (Fig. 1) is very similar to that of the arsenopyrite standard measured by Savage et al. (2000), suggesting that the local environment of As is indeed very close to that of arsenopyrite.

To reveal the As local structure quantitatively, EXAFS refinements were performed using as starting models the same arsenopyrite structure reported in Savage et al. (2000) or the model proposed by Blanchard et al. (2007). The results showed that it is indeed possible to obtain good matches with experimental data by using both models (see Fig. A.3 and Table A.1) (indeed, statistical indicators (such as the reduced χ-square) suggest that Blanchard's model is more suitable to reproduce the experimental data, because structural refinement can be successfully performed using less atomic contributions, and hence less free parameters). This result indicates that EXAFS is not able to distinguish between arsenopyrite inclusions in a pyrite matrix and As substitution resulting in a solid solution because the local structure of As in the two configurations (arsenopyrite and $FeS_{2-x}As_x$ solid solution) is very close.

Se K-edge: The XANES spectra of eleven samples (Table 1) reacted at different pH are reported in the left panel of Fig. 2 together with the spectra of the Se reference compounds ($FeSeO_3$, Na_2SeO_3, amorphous (red) Se(0), crystalline (grey) Se(0), FeSe, and $FeSe_2$). Since only slight differences in the spectral features were observed at different reaction times (7, 21, and 34 days), only spectra at the longest reaction time are shown in Fig. 2 and will be discussed in the following (XANES spectra at different reaction times are shown in Fig. A.4).

Spectra of samples obtained at pH > 5.65 (6.10, 6.94, and 8.65) show different features compared to that of samples obtained at lower pH (5.05 and 5.65), suggesting the presence of different reaction products (also see Fig. A.4). The absorption edge energy positions of all samples indicate that Se(IV) was reduced after reaction with As-rich pyrite. The analysis of the edge position cannot help distinguish between Se(0), Se(-I) and Se(-II), because the energy shifts between these oxidation states are small (<0.5 eV) and comparable with the resolution of the data (Charlet et al., 2012). For this reason, PCA and LSF were applied to XANES spectra to help unravel the reaction products. PCA reported a minimum of the indicator function (IND) in correspondence to three components, while the spectra were found to be satisfactorily reconstructed using two components only. In addition, the eigenvalues and the variance indicate that one single component is mainly responsible for the variation of the spectra. This information suggests that up to three chemical species contribute to the XANES spectra, but one is largely predominant over the others. Target transformation using the reference spectra suggested amorphous Se(0), $FeSe_2$, and $FeSeO_3$ as the best reference candidates, while the same procedure indicates that FeSe and Na_2SeO_3 can be ruled out (Fig. 2 and Table A.2).

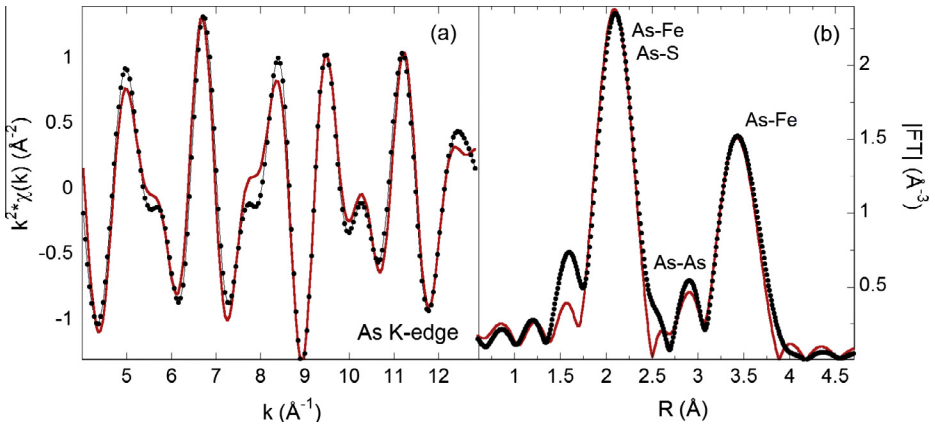

Fig. 1. Left panel: back Fourier transformed (1–4 Å) As K-edge EXAFS signal of the As-rich pyrite sample. Right panel: Fourier transform (4–13 $Å^{-1}$), Gaussian window) of the signals shown in left panels. The Fourier transform is k^2-weighted and is not corrected for the phase shift. The coordination shells contributing to the fits are labeled. In both panels points represent experimental data and solid lines the fit curves. The refinement was performed using the model proposed by Blanchard et al. (2007). Refer to Table A.1 for the refined structural parameters.

Table 1
Summary of the XANES and XPS results. Compositional values are derived from LSF results on XANES spectra. Also reported is the concentration sum (Σ), which is close to 100% for all samples, and the value of the reduced χ−square (χ_ν^2), both indicating good matches to the experimental spectra. The error on the concentrations is estimated to be around 10–15%. The occurrence or lack of the Se(0), Se(IV), and Fe^{3+} XPS signature peaks is indicated by 'Yes' or 'No', respectively.

pH	Reaction time (days)	XANES					XPS		
		Se(0) red%	$FeSeO_{3\%}$	$FeSe_{2\%}$	Σ	$\chi_\nu^2 \cdot 10^3$	Se(0)	Se(IV)	Fe^{3+}
5.05	7	100	0	0	100	0.99	Yes	No	No
	21	100	0	0	100	0.97			
	34	100	0	0	100	1.17			
5.65	7	100	0	0	100	1.05	Yes	No	No
	21	100	0	0	100	1.12			
	34	100	0	0	100	0.96			
6.10	7	95	7	0	102	0.85	No	No	Yes
	21	96	5	0	101	0.79			
	34	92	9	0	101	0.73			
6.94	44	91	11	0	102	0.29	Yes	No	Yes
8.65	44	95	7	0	102	0.31	Yes	No	Yes

Linear Square Fits using the three best candidates suggested by PCA (Se(0), $FeSe_2$, and $FeSeO_3$) confirmed that amorphous Se(0) is the dominant phase in samples reacted at pH ⩽ 5.65 (5.05 and 5.65), while, in samples reacted at higher pH (6.10, 6.94, and 8.65), possible presence of $FeSeO_3$ was estimated to be in the range 5–10%. However, since the error on the relative compositions calculated by the LSF procedure is around 10–15%, the actual presence of $FeSeO_3$ remains uncertain. It is worth noting that in all solutions, $FeSeO_3$ ($K_s = 10^{-9.99}$ (Seby et al., 2001)) was always below saturation (SI < −0.3 at pH 6.10, while SI < −1.1 at pH 6.94). Nevertheless, because the isoelectric point of pyrite is around pH 2.0, the negatively charged surface at pH > 2.0 can adsorb aqueous Fe^{2+} (Descostes et al., 2010; Weerasooriya and Tobschall, 2005). Therefore, precipitation of $FeSeO_3$ becomes possible due to the high Fe^{2+} concentration at the interface. LSF results are reported in Table 1.

EXAFS refinements were performed on the extended part of the absorption spectra to unravel the local structure around Se. The extracted structural parameters of selected samples and reference compounds are reported in Table 2. A first coordination shell of two Se atoms at a distance of 2.34 Å is observed in samples reacted at pH 5.05 and 6.10. This distance is shorter than for crystalline (grey) Se(0) (2.37 Å), but in excellent agreement with the amorphous (red) Se(0) standard (Table 2). Two weak selenium next neighbor shells were observed at about 3.1 and 3.7 Å. The short one matches the Se coordination shell of $FeSe_2$ (Table 2), while the longer is in agreement with the Se shells observed in the red and grey Se(0) structures (3.77 and 3.71 Å, respectively) and in the FeSe standards (3.74 Å). Considering the LSF results, the long Se coordination was attributed to the Se(0) structure.

The low coordination numbers (CN) of these shells (about 0.5) indicate the rather amorphous or nanocrystalline character of the Se(0) phase in these samples. Samples reacted at pH 6.94 and 8.65 do not show coordination shells higher than the first, revealing that the dominant phase is constituted by amorphous Se(0).

It has to be noted that the possible contribution from an iron shell arising from a small amount (5–10%) of $FeSeO_3$ or iron selenides would be hindered by the stronger contributions from the Se shells (Charlet et al., 2012). Therefore, the presence of phases other than the dominant Se(0), cannot be confirmed by EXAFS refinements.

For samples reacted at pH 6.07 and 7.51 (with addition of 0.10 and 0.08 mM $FeCl_2$, respectively), XANES-EXAFS analyses indicate the formation of amorphous Se(0), along with large amounts of $FeSeO_3$ (Fig. A.5 and Table A.3).

3.2. X-ray photoemission spectroscopy

The Fe 2p, S 2p, and Se 3d (or Fe 3p) XPS spectra of the fresh (before reaction with Se(IV)) and Se(IV)-reacted As-rich pyrite are shown in Figs. 3 and A.6. The spectra of the fresh As-rich pyrite

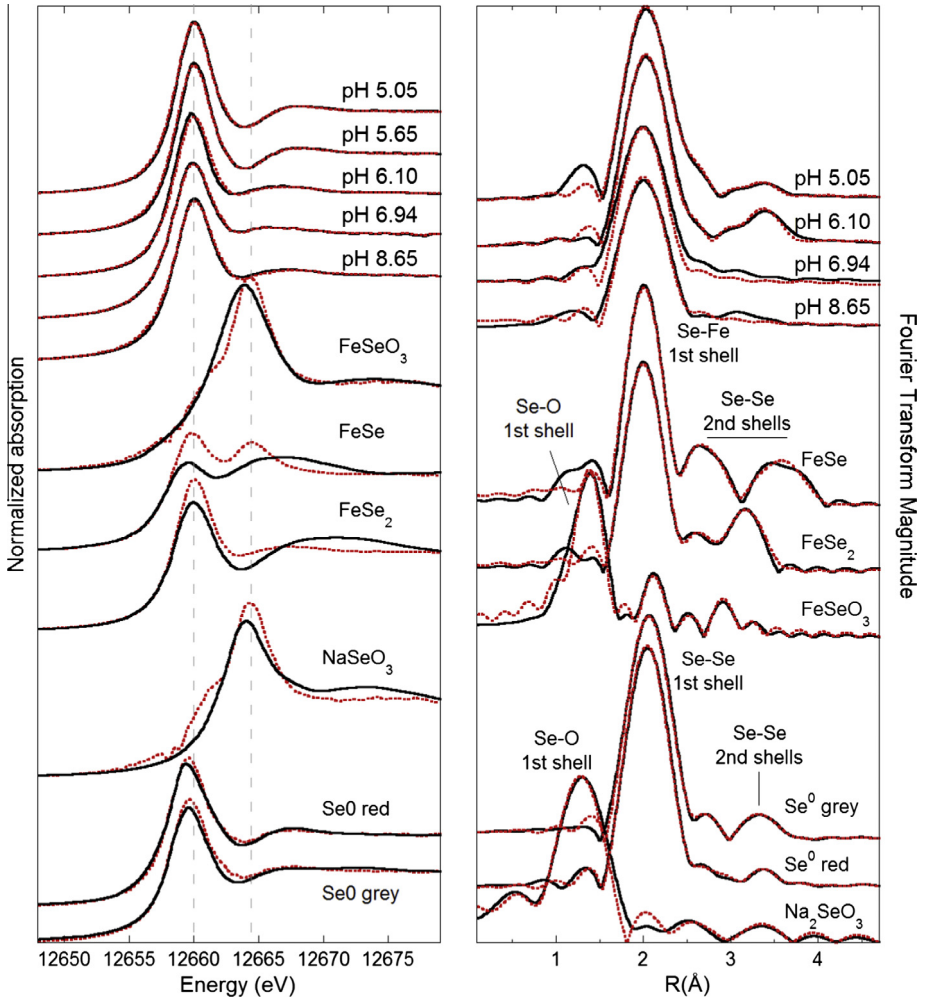

Fig. 2. Left panel: K-edge XANES spectra of pyrite reacted with Se(IV) samples and of the reference compounds (solid lines are experimental data; dotted lines are PCA reconstruction of the samples' spectra using two components; for reference samples dotted lines represent target transformation curves). Right panel: Fourier transforms moduli of the EXAFS signals (k-range: 4–12 $Å^{-1}$, Gaussian window, not corrected for the phase shift) of selected samples and reference compounds (solid lines are experimental data; dotted lines are fits).

exhibit intense peaks at 708.0 eV and 163.3 eV, in the Fe $2p_{3/2}$ and S $2p_{3/2}$ regions, characteristic of stoichiometric FeS_2. The high energy tail of the Fe $2p_{3/2}$ spectrum can be fitted with the component at 709.5 eV, which matches the Fe $2p_{3/2}$ component of Fe(II)–O (708.5–709.5 eV) and the multiplet peaks (709.1–711.4 eV) of Fe(III)–S (Schaufuss et al., 1998). The Fe(II)–O feature can be assigned to surface hydroxylation processes (Eggleston et al., 1996), or to hydrated Fe^{2+} sorbed at the pyrite surface (Descostes et al., 2010), while the presence of Fe(III)–S may originate from the breaking of Fe–S bonds at the surface, with an electron being transferred from iron to sulfur, and inducing the formation of Fe^{3+} surface sites (Elsetinow et al., 2000; Murphy and Strongin, 2009).

After reaction with Se(IV), additional Fe 2p and S 2p peaks, which can be attributed to n-type pyrite, appear. Pyrite is a semicondutor with either n-type or p-type properties, and within a single pyrite specimen, there may exist zones exhibiting alternate n- and p-type behavior. Typically p-type pyrites exhibit low conductivities and are As-rich, whereas relatively highly conducting n-type pyrites are typically As-poor (Rimstidt and Vaughan, 2003). The presence of n-type pyrite after reaction can be ascribed to the loss of arsenic in the pyrite phase, in agreement with the excessive arsenic-impurity leaching observed (see Section 3.3).

Compared to the fresh As-rich pyrite, the sample reacted at pH 6.10 shows an extra peak at 711.8 eV. Similar peaks were observed at 711.2 eV for the samples reacted at pH 6.94 and 8.65. For the samples reacted at pH 6.07 and 7.51 with adding extra Fe^{2+}, intense peaks at 711.1 and 711.7 eV were observed. These peaks can be attributed to oxygen-bonded ferric ion and suggest the formation of Fe(III)-(oxyhydr)oxide precipitation after reaction, in agreement with the lack of aqueous iron in these reactors after reaction (Tables B.1 and B.3).

The S 2p spectra were fitted with S $2p_{3/2}$ and S $2p_{1/2}$ spin orbit doublets, with a fixed 2:1 intensity ratio and a 1.18 eV energy separation. The sample reacted at pH 6.94 shows three types of pyrite doublets, and it also shows S $2p_{3/2}$ peak at 165.2 eV, which is compatible with the binding energy range of sulfite (Swartz et al., 1971). Apart from the S 2p peak from disulfide in pyrite, no other sulfur species were detected on the other samples.

Since the photoelectrons of selenium with low oxidation state (0, -I and -II) interfere with the photoelectrons of iron, the Se 3d spectra were deconvolved in Se 3d and Fe 3p peaks. For the samples reacted at pH 5.05, 5.65, 6.94, and 8.65, the Se $3d_{5/2}$ peaks occur at 55.8, 56.0, 55.5, and 55.9 eV, respectively, well matching the Se(0) reference at 55.6 eV (Fig. A.7). For the sample reacted at pH 6.10, peaks corresponding to selenium with low oxidation state (0, -I and -II) are too weak to be detected, due to the overlap with the Fe 3p peaks. For the samples reacted at pH 6.07 and 7.51 with adding extra Fe^{2+}, two selenium components contribute to each Se 3d peak. The lower energy contributions at 55.5 and 55.7 eV are

Table 2
Structural parameters obtained from EXAFS refinements (S_0^2, amplitude reduction factor; CN: coordination numbers; *R*: atomic distances; σ^2: Debye–Waller factors). With the exception of amorphous (red) Se(0), all CN of standards compounds were kept fixed to the crystallographic values. Common Debye–Waller factors are indicated by the sign "+". The numbers within parentheses represent the error on the last digit.

	1st shell			2nd shells			S_0^2	χ_v^2
	CN	*R* (Å)	σ^2 (Å$^2 \cdot 10^3$)	CN	*R* (Å)	σ^2 (Å$^2 \cdot 10^3$)		
Standards								
Se(0)	2 Se	2.373(3)	3.5(3)	4 Se	3.40(3)	22(4)	1.02(6)	0.94
Grey								
				2 Se	3.71(2)	13(3)		
Se(0)	2 Se	2.346(3)	3.6(3)	0.6(5) Se	3.77(4)	7(5)	1.09(6)	0.87
Red				0.2(4) Se	3.99(9)	5(4)		
$FeSe_2$	3 Fe	2.376(2)	4.5(1)	1 Se	2.558(4)	4.5(1)	0.89(4)	0.99
				4 Se	3.13(1)	4(1)		
				4 Se	3.29(1)	+		
				2 Se	3.43(2)	4(1)		
				2 Se	3.58(4)	+		
				1 Fe	3.81(7)	3(2)		
				2 Fe	3.97(2)	+		
FeSe	4 Fe	2.399(4)	2.4(4)	8 Se	3.74(2)	8.4(2)	0.74(4)	0.87
				4 Se	3.94(2)	2.4(8)		
				12 Fe	4.46(2)	11(2)		
$FeSeO_3$	3 O	1.717(8)	2.2(8)	3 O	2.46(1)	1.2(9)	0.8(1)	0.84
				1 O	2.64(2)	+		
				4(1) Fe	2.81(2)	8(3)		
				4(1) Fe	3.01(2)	+		
Na_2SeO_3	3 O	1.700(2)	3.7(3)	2 Na	3.12(5)	5(3)	1.0(1)	0.74
				2 Na	3.36(6)	4(3)		
Samples								
pH 5.05	1.8(7) Se	2.339(2)	2.7(2)	0.5(3) Se	3.08(1)	2(1)	0.93(4)	4.1
				0.3(2) Se	3.77(2)	+		
pH 6.01	1.7(2) Se	2.342(5)	3.7(5)	0.3(2) Se	3.11(4)	4(2)	0.93(3)	1.8
				0.8(5) Se	3.70(2)	+		
pH 6.94	2 Se	2.333(5)	5.6(5)				1.09(3)	1.79
pH 8.65	2 Se	2.335(8)	5.5(7)				1.01(1)	1.97

assigned to Se(0), while the higher energy signal at 59.1 and 59.6 eV are attributed to the unreduced Se(IV). The latter may originate from the adsorption of Se(IV) by Fe(III)-(oxyhydr)oxide or the surface precipitation of $FeSeO_3$, in agreement with XANES-EXAFS results (Fig. A.5 and Table A.3).

3.3. Pyrite dissolution

Oxidative dissolution of pyrite by dissolved oxygen and ferric iron has intensively been studied (Moses and Herman, 1991; Rimstidt and Vaughan, 2003; Williamson and Rimstidt, 1994), and results demonstrated that the oxidation does not oxidize iron, but sulfur. In this study, the iron concentration determined by phenanthroline method, with and without the reduction step by hydroxylamines, was the same. Therefore, the results of the works cited above also apply to pyrite oxidation by Se(IV) (i.e., all the measured dissolved iron were in the form of Fe^{2+}).

In batch experiments at pH 5.05 and 5.65, aqueous iron and sulfur increased along with a slight increase of the pH. These facts are consistent with the reduction of Se(IV) to Se(0) (Kang et al., 2011). At pH 5.05 and 5.65, the $\Delta[S]_{tot}/\Delta[Fe]_{tot}$ ratios, obtained from the slopes of the linear regression of [S] vs. [Fe], were 0.28 and 0.47, respectively. The $\Delta[Se]_{tot}/\Delta[Fe]_{tot}$ ratios, obtained in the same way, were 0.88 and 1.04 at pH 5.05 and 5.65, respectively (Fig. 4). The $\Delta[S]_{tot}/\Delta[Fe]_{tot}$ ratios are much lower than the values reported in previous works for pyrite oxidative dissolution. For pyrite oxidized by oxygen, Descostes et al. (2004) reported values ranging from 1.25 at pH 1.5 to 1.6 at pH 3, while Kamei and Ohmoto (2000) obtained values in the range 0.93–2.00 for the same reaction at pH 5.7 ± 0.3.

The significant sulfur deficit observed in this study suggests the formation of other sulfur species. Perchloroethylene extraction and subsequent quantitative analysis by high-performance liquid chromatography (HPLC) revealed that 0.156, 0.178, and 0.074 mmol of elemental sulfur were formed at pH 5.05, 5.65, and 6.10, respectively (Table B.4). These values are close to the amounts of total aqueous sulfur detected at these pH values (0.146, 0.201, and 0.203 mmol, respectively). Many authors reported sulfur deficit during pyrite dissolution (Descostes et al., 2004; Kamei and Ohmoto, 2000; Paschka and Dzombak, 2004), but did not observe S^0 as a reaction product.

At pH 6.10, the $\Delta[S]_{tot}/\Delta[Fe]_{tot}$ and $\Delta[Se]_{tot}/\Delta[Fe]_{tot}$ ratios were measured to be 0.77 and 1.82, respectively. Note that the iron concentration slightly decreased or remained constant from 502.5 h to 645.5 h, although a considerable amount of Se(IV) was reduced during this time. The slight decrease of iron was coupled with a decrease in $\Delta[Se]_{tot}/\Delta[S]_{tot}$ ratio (from 2.41 to 2.00) (Fig. 5), indicating an additional release of sulfur. In a previous work we found that, in the presence of unreduced selenite, Se(0) rather than iron selenides can be formed on Fe(II)-bearing minerals (Kang et al. 2013). Therefore, the iron decrease can be attributed to the formation of $Fe(OH)_3$ (Kang et al., 2011), in agreement with XPS results (Fig. A.6), while, at the same time, additional pyrite was decomposed through reaction (1) leading to the release of more aqueous S (see Section 3.4 in the following).

At pH 6.94 and 8.65, the formation of Fe(III)-(oxyhydr)oxide is kinetically favored (Figs. 3 and A.6) due to large amount of Se(IV) present in the solution. The precipitation of Fe(III)-(oxyhydr)oxide consumed nearly all the aqueous ferrous. This was also observed in reactions at pH 6.07 and 7.51 (Figs. 3 and A.6), as most of the extra added Fe^{2+} was consumed (Table B.3). On the other hand, Fe^{2+}-free solution could limit the formation of $FeSe_2$, as suggested by the XAS and XPS results.

3.4. Reaction pathway

Luther (1997), Kelsall et al. (1999), and Rimstidt and Vaughan (2003) proposed a pathway for pyrite oxidation involving

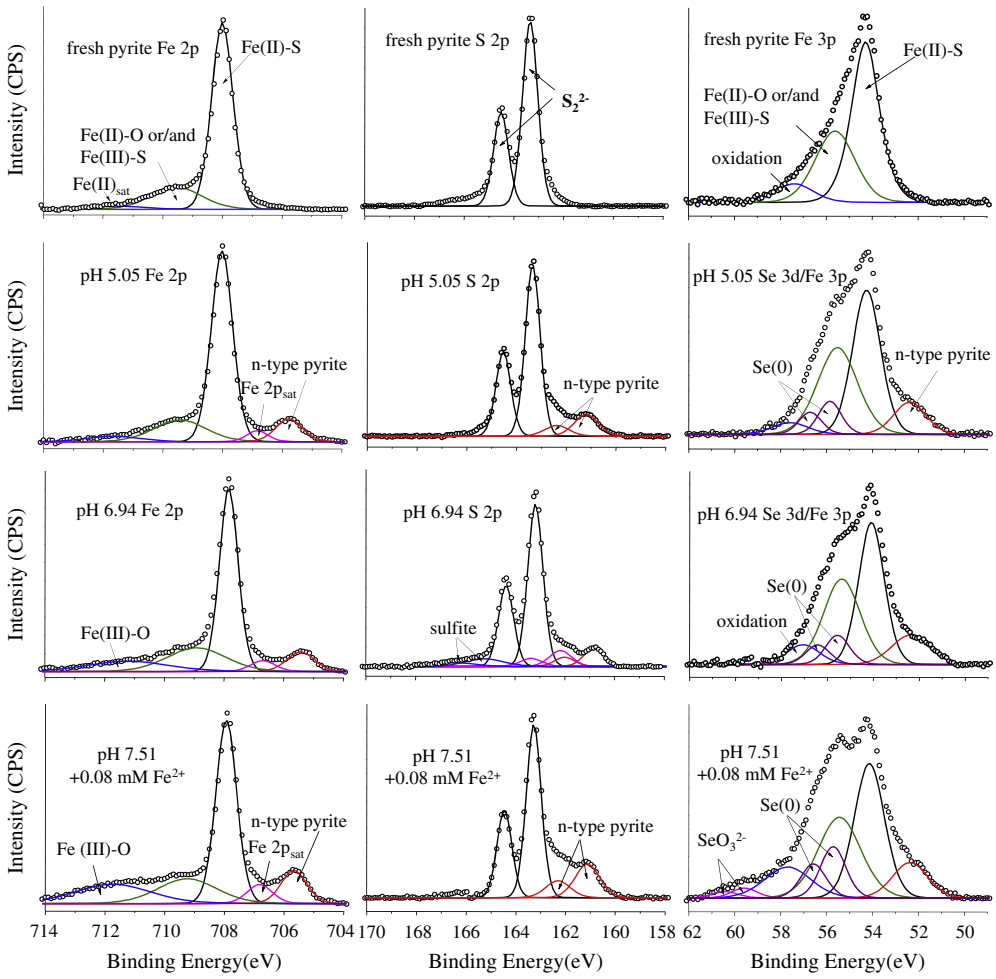

Fig. 3. Fitted Fe 2p, S 2p, and Se 3d (or Fe 3p) XPS spectra for the fresh (before reaction with Se(IV)) pyrite and Se(IV)-reacted pyrite at pH 5.05, 6.94, and 7.51 (with adding 0.08 mM Fe^{2+}). N-type pyrite represents the split pyrite phase due to the loss of arsenic-impurity.

thiosulfate ion ($S_2O_3^{2-}$). The possible formation of thiosulfate after pyrite oxidation by selenite can be represented by the following reaction:

$$FeS_2 + 1.5H^+ + 1.5HSeO_3^- = Fe^{2+} + S_2O_3^{2-} + 1.5Se^0 + 1.5H_2O \quad (1)$$

Alternatively, selenite can interact with thiosulfate, leading to the formation of seleno-polythionates, such as selenotrithionate, $Se(SO_3)_2^{2-}$ or selenopentathionate, $Se(S_2O_3)_2^{2-}$ (Ball and Milne, 1995; Rahim and Milne, 1996). These soluble Se(0) containing species could further decompose with the release of elemental selenium and sulfate, a process known to be catalyzed by thiosulfate. In the present study, capillary electrophoresis method was used to check for $S_2O_3^{2-}$. However, the detection of thiosulfate was prevented because of its high instability, and extra $S_2O_3^{2-}$ added to the solution was oxidized to SO_4^{2-} within a few minutes upon exposing to air. Therefore, the total sulfur, which was measured by ICP-OES, is assumed to be in the form of SO_4^{2-} and/or SO_3^{2-} (in agreement with XPS results), although thiosulfate and seleno-polythionates may have occurred. In acidic conditions, thiosulfate may disproportionate into either tetrathionate, or elemental sulfur and sulfite, following the reactions (Williamson and Rimstidt, 1993; Xu and Schoonen, 1995):

$$8S_2O_3^{2-} + H^+ \rightarrow S_8 + HSO_3^- + 7SO_3^{2-} \quad (2)$$

$$2S_2O_3^{2-} + 2Fe^{3+} \rightarrow FeS_2O_3^+ + FeS_2O_3^+ \rightarrow S_4O_6^{2-} + 2Fe^{2+} \quad (3)$$

Williamson and Rimstidt (1993) pointed out that ferric iron is critical in these two reactions. Eq. (2) indicates that elemental sulfur accounts for 50% of the total reacted thiosulfate through decomposition, which can explain the formation of S^0 observed at pH 5.05 and 5.65. Moreover, XPS surface analysis on samples reacted at pH 6.94 (Fig. 3) suggested the presence of sulfite species, suggesting reaction (2) as an effective pathway in the present study. However, thiosulfate pathway alone cannot adequately describe the dissolution process in our experiments, because the sum of the measured aqueous sulfur and solid S^0 was less than the amount of the released Fe^{2+}; therefore, significantly deviating from the Fe/S ratio in our As-rich pyrite.

Besides the thiosulfate pathway, polysulfide pathway is another important reaction mechanism that controls the dissolution of metal sulfides. Unlike the thiosulfate pathway for acid-insoluble pyrite, the sulfide–polysulfide–elemental sulfur pathway is prevalent for acid-soluble metal sulfides such as arsenopyrite, pyrrhotite, mackinawite, chalcopyrite, sphalerite and galena. In this group of metal sulfides, the chemical bond between metal and sulfur moiety can be broken by both oxidant (i.e., Fe^{3+}) and proton attack. In the course of polysulfide oxidation, more than 90% of the sulfide moiety of a metal sulfide is transformed to elemental sulfur (Donati and Sand, 2007). The As-rich pyrite used in this study contains 2.56 wt% arsenic-impurity ($FeS_{2.08}As_{0.043}$), and excessive arsenic leaching was observed. At pH 5.05, 5.65, and 6.10, the aqueous As/S ratios were equal to 0.85, 0.56 and 0.38, and aqueous As/Fe ratios were equal to 0.24, 0.27, and 0.31,

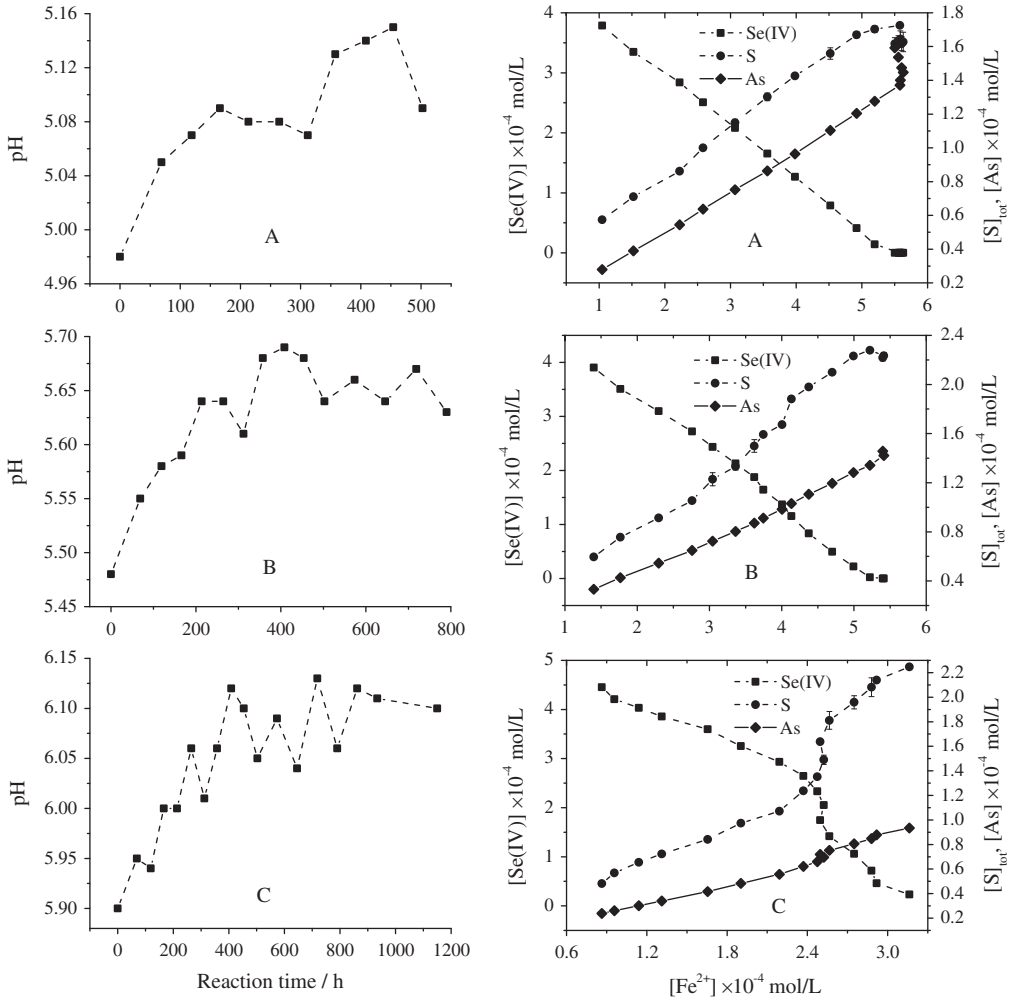

Fig. 4. Plots of the analytical results reported in Table B.1. Left panels show the variation of the solution pH; right panels report the variation of [Se(IV)], $[S]_{tot}$, and [As] vs. $[Fe^{2+}]$.

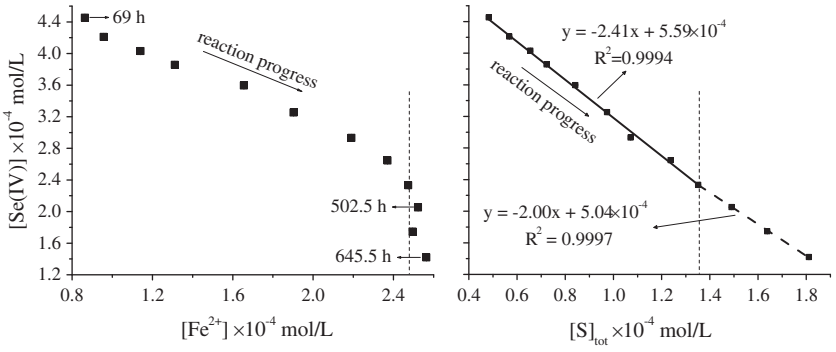

Fig. 5. Left panel: Se(IV) concentration vs. Fe^{2+}. Right panel: [Se(IV)] vs. $[S]_{tot}$ at pH 6.10.

respectively (Fig. 4 and Table B.1). It is commonly accepted that As in pyrite oxidizes more readily than Fe (Huggins et al., 2002), and that As-rich pyrite is more reactive than pyrite without As (Abraitis et al., 2004). Blanchard et al. (2007) suggested that during the dissolution process, the formation of sulfur vacancies would preferentially occur in the neighboring of arsenic, which could be partly responsible for the faster oxidation of As-rich pyrite.

Oxidation of arsenopyrite by Se(IV) can be described by Eqs. (4) and (5), which respectively lead to SO_4^{2-} or S^0 as oxidation products.

$$4FeSAs + 11H^+ + 11HSeO_3^- = 4Fe^{2+} + 4SO_4^{2-} + 4H_3AsO_3 + 11Se^0 + 5H_2O \quad (4)$$

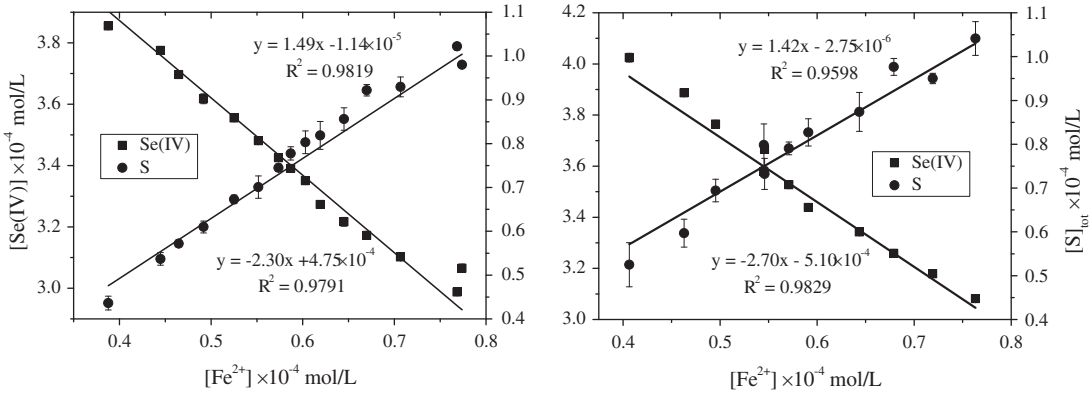

Fig. 6. Solution results for the control experiments at pH 4.26 (left panel) and 4.50 (right panel).

$$4FeSAs + 13H^+ + 5HSeO_3^- = 4Fe^{2+} + 4S^0 + 4H_3AsO_3 + 5Se^0 + 3H_2O \quad (5)$$

The $\Delta[S]_{tot}/\Delta[Fe]_{tot}$ ratio in reaction (4) is 1; therefore, this reaction cannot account for the aqueous sulfur deficit in this study. Other studies observed S^0 as the main product of arsenopyrite oxidation (McGuire and Hamers, 2000; McGuire et al., 2001). The $\Delta[Se]_{tot}/\Delta[Fe]_{tot}$ ratio of reaction (5) is 1.25, which is close to the observed values. If we assume that As in our pyrite sample has the same local environment as in arsenopyrite (as suggested by Blanchard et al. (2007) and supported by our As-edge XAS data), the As-impurity leaching can be described by Eq. (5), implying that the polysulfide-elemental sulfur pathway plays a relevant role in the reduction of Se(IV) by As-rich pyrite. From the observed As/S ratios, it was estimated that Eq. (5) contributed to Se(IV) reduction for ~26% and ~19%, at pH 5.05 and 5.65, respectively. The rest of the reduction can be attributed to Eqs. (1) and (2). The observed ratios of $\Delta[S]_{tot}/\Delta[Fe]_{tot}$, $\Delta[As]_{tot}/\Delta[S]_{tot}$, $\Delta[Se]_{tot}/\Delta[Fe]_{tot}$, and $\Delta[Se]_{tot}/\Delta[As]_{tot}$ at pH 5.05 and 5.65 are comparable to the theoretical values (0.35, 0.84, 1.43, and 4.8, at pH 5.05, and 0.39, 0.56, 1.45, and 6.58, at pH 5.65), confirming the above assumption. It is worth noting that due to the acid-soluble property of arsenopyrite, the contribution of Eq. (5) to Se(IV) reduction decreased with increasing pH.

The release of the As-impurity via arsenopyrite oxidation can partially account for the pH increase (H^+ is also consumed in Eqs. (1) and (2)), even when $Fe(OH)_3$ was formed at pH 6.07, 6.94 and 7.51 (Table B.3) according to the following reaction:

$$2FeSAs + 3H^+ + 3HSeO_3^- + 3H_2O = 2S^0 + 2H_3AsO_3 + 3Se^0 + 2Fe(OH)_3 \quad (6)$$

The control experiments further confirm the importance of arsenic impurity on pyrite dissolution pathway. As can be seen from Fig. 6, interaction of Se(IV) with the As-free pyrite reference resulted in $\Delta[S]_{tot}/\Delta[Fe]_{tot}$ and $\Delta[Se]_{tot}/\Delta[Fe]_{tot}$ ratios of 1.49 and 2.30 at pH 4.26, and 1.42 and 2.70 at pH 4.50, respectively. These values are much higher than that observed for As-rich pyrite (reported above), suggesting that, for As-free pyrite, acid-insoluble pyrite dominated the Se(IV) reduction. In this framework, the $S_2O_3^{2-}$ initially released (Eq. (1)) was partially oxidized to SO_4^{2-} (Eq. (7)). The remaining $S_2O_3^{2-}$ was decomposed to S^0 and SO_3^{2-} via Eq. (2), and SO_3^{2-} was further oxidized to SO_4^{2-} (Eq. (8) represents the net reaction).

$$FeS_2 + 1.5H^+ + 3.5HSeO_3^- = 2SO_4^{2-} + Fe^{2+} + 3.5Se^0 + 2.5H_2O \quad (7)$$

$$FeS_2 + 2H^+ + 2HSeO_3^- = SO_4^{2-} + S^0 + Fe^{2+} + 2Se^0 + 2H_2O \quad (8)$$

If reactions (7) and (8) account respectively for 55% and 45% of the Se(IV) reduction, the theoretical ratios of $\Delta[S]_{tot}/\Delta[Fe]_{tot}$ and $\Delta[Se]_{tot}/\Delta[Fe]_{tot}$ would be 1.41 and 2.62, respectively, in line with the observed values for As-free pyrite.

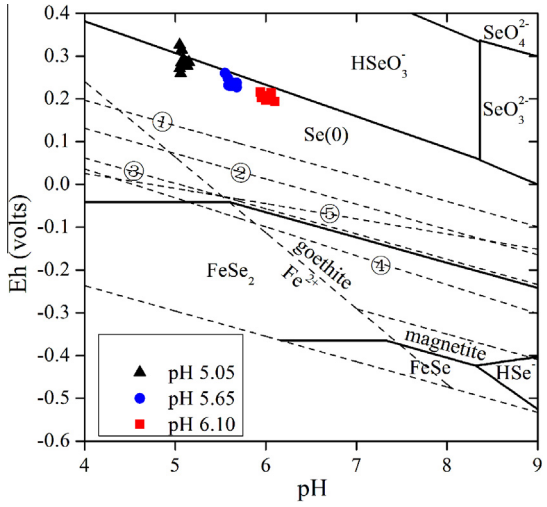

Fig. 7. Eh–pH diagram for the Se–Fe–O–H_2O system overlaid with Eh–pH relationships for the Fe–S–O–H_2O system. Continuous black lines correspond to final experimental conditions ($\Sigma Se = 10^{-7}$ M, $\Sigma Fe = 5 \times 10^{-4}$ M). The red dotted line indicates the equilibrium between Fe^{2+} and goethite, and the blue one represents the equilibrium between goethite and magnetite. The point's clusters denote the experimental pH and Eh conditions. Dotted lines ($\Sigma S = 2 \times 10^{-4}$ M, $\Sigma Fe = 5 \times 10^{-4}$ M, $\Sigma As = 1 \times 10^{-4}$ M) are for ①: $FeS_2 + 3H_2O = Fe^{2+} + SO_3^{2-} + S(0) + 6H^+ + 6e^-$; ②: $FeS_2 + 3H_2O = Fe^{2+} + S_2O_3^{2-} + 6H^+ + 6e^-$; ③: $FeS_2 + 4H_2O = Fe^{2+} + SO_4^{2-} + S(0) + 8H^+ + 8e^-$; ④: $FeS_2 + 8H_2O = Fe^{2+} + 2SO_4^{2-} + 16H^+ + 14e^-$; ⑤: $FeAsS + 3H_2O = Fe^{2+} + S^0 + H_3AsO_3(aq) + 3H^+ + 5e^-$. (For interpretation of the references to colour in this figure legend, the reader is referred to the web version of this article.)

3.5. Thermodynamic calculations

The Eh–pH predominance diagram for selenium in Fe–S–O–H_2O system (Chivot, 2004; Olin et al., 2005) is shown in Fig. 7. The thermodynamic data for arsenopyrite and $H_3AsO_3(aq)$ are from Pokrovski et al. (2002). The redox potentials of all samples reacted with Se(IV) at pH 5.05–6.10 were in the Se(0) stability field. The reduction of Se(IV) by pyrite is initiated by an adsorption reaction, followed by slow reduction, or by a simultaneous reductive adsorption at the pyrite/water interface (Bruggeman et al., 2005). The redox potential at the interface can be represented by pyrite/arsenopyrite dissolution, and is represented by lines ①, ②, ③, ④, and ⑤ in Fig. 7. Lines ① and ② indicate that, when SO_3^{2-} and S^0, or $S_2O_3^{2-}$ are the reaction products of pyrite oxidation, Se(0) should be the only Se reaction product at all pH values. On the other hand,

when SO_4^{2-} and S^0 are observed after pyrite oxidation, line ③ suggests that $FeSe_2$ should be the predominant Se reaction product at pH > 5.61, and Se(0) at pH < 5.61. If only SO_4^{2-} is observed after pyrite oxidation, line ④ suggests that $FeSe_2$ becomes the predominant product at pH > 5.15. Finally, line ⑤ indicates that, when S^0 is observed after arsenopyrite oxidation, Se(0) is the only Se reaction product at all pHs. Therefore, the formation of $FeSe_2$ on As-rich pyrite at pH 5.65, 6.10, 6.94, and 8.65 is thermodynamically allowed only when SO_4^{2-} is produced, while Se(0) is expected to be the predominant species in presence of SO_4^{2-} and at pH 5.05. Nevertheless, due to the relatively low reactivity of the As-rich natural pyrite and the oxidizing environment generated by the added Se(IV) (at pH > 5.87 lines ③ and ④ are in the stability area of goethite), the formation of Se(0) is kinetically favored at the early stage of the reaction. In a previous work we observed that iron selenides can be oxidized to Se(0) by Se(IV) with fast kinetics (Kang et al., 2013). A recent study further indicated that $FeSe_2$ is more reactive than pyrite towards Fe^{3+} and Se(IV) (Ma et al., 2014). Therefore, in presence of unreduced Se(IV), Se(0) rather than iron selenides, can be formed. Note that, bulk Se(0), which has low solubility is expected to form due to the slow reaction (colloidal Se(0) tends to aggregate). This can kinetically inhibit the dissolution required for the further transformation into more stable species ($FeSe_2$), leading the system to undergo redox disequilibrium in short-term laboratory experiments. This may be one of the reasons why in this study, even after the depletion of the aqueous Se(IV) at pH 5.65, only Se(0) is observed, in line with previous works (Breynaert et al., 2008, 2010). A previous study on more reactive nano-sized pyrite/greigite mixture revealed the formation of a large amount of $FeSe_2$, confirming the critical effect of reaction kinetics on the reaction products (Charlet et al., 2012).

4. Conclusions

Reduction of selenite by As-rich natural pyrite was investigated as a function of reaction time and ferrous content in the pH range 5.05–8.65. Se(0) was found to be the unique reduction product at all the studied pH values, while small amount of $FeSeO_3$ might have been formed along with Se(0) at pH $\geqslant$ 6.10. At pH $\geqslant$ 6.07, the precipitation of Fe(III)-oxyhydroxide is kinetically favorable, and it consumed nearly all the aqueous iron (including the extra added Fe^{2+}), thereby inhibiting the formation of the thermodynamically most stable $FeSe_2$. The speciation studies indicate a strong kinetic dependence of the reaction products, leading to severe redox disequilibrium in short-term laboratory experiments. The results of this work show that, when aqueous Se(IV) is used as oxidant, pyrite oxidation does not produce acid under acidic to nearly neutral conditions. This implies that pyrite can potentially be a good reductant to immobilize the redox-sensitive radionuclides like ^{79}Se in long-term nuclear waste repository.

Natural pyrite generally holds minor elements, such as As. The results of this study suggest that oxidation of As-rich pyrite by aqueous Se(IV) involves multiple complex and concurrent reactions. The reported results also confirm that As local environment in our As-rich pyrite sample is very close to arsenopyrite, and that, in addition to the thiosulfate pathway, the release of the As-impurity via arsenopyrite oxidation by means of polysulfide-elemental sulfur pathway plays a relevant role in the dissolution of As-rich pyrite.

Acknowledgements

The research leading to these results has received funding from the European Union's European Atomic Energy Community's (Euratom) Seventh Framework Programme FP7/2007–2011 under Grant agreement No. 212287 (RECOSY project), and the China Postdoctoral Science Foundation (Grant No. 2013M530013). The authors are grateful to Italian beamline (BM8 – GILDA) at the European Synchrotron Radiation Facility (ESRF) of Grenoble (France), and in particular to Dr. Francesco D'Acapito and Angela Trapananti for providing beamtime and assistance during XAS measurements. We also thank Jean-Marc Greneche (Institut des Molécules et Matériaux du Mans, Université du Maine, Le Mans, France) for recording Mössbauer spectra. The authors gratefully acknowledge Delphine Tisserand (ISTerre, University of Grenoble I) for ICP analyses and experimental assistance.

Appendix A. Supplementary material

Supplementary data associated with this article can be found, in the online version, at http://dx.doi.org/10.1016/j.apgeochem.2014.05.018.

References

Abraitis, P.K., Pattrick, R.A.D., Vaughan, D.J., 2004. Variations in the compositional, textural and electrical properties of natural pyrite: a review. Int. J. Miner. Process. 74, 41–59.
Ankudinov, A.L., Ravel, B., Rehr, J.J., Conradson, S.D., 1998. Real-space multiple-scattering calculation and interpretation of X-ray-absorption near-edge structure. Phys. Rev. B 58, 7565–7576.
Baeyens, B., Maes, A., Cremers, A., Henrion, P.N., 1985. Insitu physicochemical characterization of Boom clay. Radioact. Waste Manage. Environ. Restorat. 6 (3–4), 391–408.
Ball, S., Milne, J., 1995. Studies on the interaction of selenite and selenium with sulfur donors. 3. Sulfite. Can. J. Chem.-Rev. Can. Chim. 73, 716–724.
Baryosef, B., Meek, D., 1987. Selenium sorption by kaolinite and montmorillonite. Soil Sci. 144, 11–19.
Bienvenu, P., Cassette, P., Andreoletti, G., Be, M.M., Comte, J., Lepy, M.C., 2007. A new determination of ^{79}Se half-life. Appl. Radiat. Isot. 65, 355–364.
Blanchard, M., Alfredsson, M., Brodholt, J., Wright, K., Catlow, C.R.A., 2007. Arsenic incorporation into FeS_2 pyrite and its influence on dissolution: a DFT study. Geochim. Cosmochim. Acta 71, 624–630.
Breynaert, E., Bruggeman, C., Maes, A., 2008. XANES-EXAFS analysis of se solid-phase reaction products formed upon contacting Se(IV) with FeS_2 and FeS. Environ. Sci. Technol. 42, 3595–3601.
Breynaert, E., Scheinost, A.C., Dom, D., Rossberg, A., Vancluysen, J., Gobechiya, E., Kirschhock, C.E.A., Maes, A., 2010. Reduction of Se(IV) in Boom clay: XAS solid phase speciation. Environ. Sci. Technol. 44, 6649–6655.
Bruggeman, C., Maes, A., Vancluysen, J., Vandenmussele, P., 2005. Selenite reduction in Boom clay: effect of FeS_2, clay minerals and dissolved organic matter. Environ. Pollut. 137, 209–221.
Charlet, L., Kang, M.L., Bardelli, F., Kirsch, R., Ghéin, A., Grèneche, J.M., Chen, F.R., 2012. Nanocomposite pyrite–greigite reactivity toward Se(IV)/Se(VI). Environ. Sci. Technol. 46, 4869–4876.
Chen, F.R., Burns, P.C., Ewing, R.C., 1999. ^{79}Se: geochemical and crystallo-chemical retardation mechanisms. J. Nucl. Mater. 275, 81–94.
Chivot, J., 2004. Thermodynamique des produits de corrosion. Sciences et Techniques Series, Andra.
Descostes, M., Vitorge, P., Beaucaire, C., 2004. Pyrite dissolution in acidic media. Geochim. Cosmochim. Acta 68, 4559–4569.
Descostes, M., Schlegel, M.L., Eglizaud, N., Descamps, F., Miserque, F., Simoni, E., 2010. Uptake of uranium and trace elements in pyrite (FeS_2) suspensions. Geochim. Cosmochim. Acta 74, 1551–1562.
Diener, A., Neumann, T., Kramar, U., Schild, D., 2012. Structure of selenium incorporated in pyrite and mackinawite as determined by XAFS analyses. J. Contam. Hydrol. 133, 30–39.
Donati, E.R., Sand, W., 2007. Microbial Processing of Metal Sulfides. Springer, P.O. Box 17, 3300 AA Dordrecht, Netherlands, pp. 36–39.
Eggleston, C.M., Ehrhardt, J.J., Stumm, W., 1996. Surface structural controls on pyrite oxidation kinetics: an XPS-UPS, STM, and modeling study. Am. Miner. 81, 1036–1056.
Elsetinow, A.R., Guevremont, J.M., Strongin, D.R., Schoonen, M.A.A., Strongin, M., 2000. Oxidation of 100 and 111 surfaces of pyrite: effects of preparation method. Am. Miner. 85, 623–626.
Fordyce, F.M., Zhang, G.D., Green, K., Liu, X.P., 2000. Soil, grain and water chemistry in relation to human selenium-responsive diseases in Enshi District, China. Appl. Geochem. 15, 117–132.
Foster, A.L., Brown, G.E., Tingle, T.N., Parks, G.A., 1998. Quantitative arsenic speciation in mine tailings using X-ray absorption spectroscopy. Am. Miner. 83, 553–568.
Gaucher, E., Robelin, C., Matray, J.M., Negral, G., Gros, Y., Heitz, J.F., Vinsot, A., Rebours, H., Cassagnabere, A., Bouchet, A., 2004. ANDRA underground research laboratory: interpretation of the mineralogical and geochemical data acquired

in the Callovian–Oxfordian formation by investigative drilling. Phys. Chem. Earth 29, 55–77.
Grambow, B., 2008. Mobile fission and activation products in nuclear waste disposal. J. Contam. Hydrol. 102, 180–186.
Guo, Z.J., Chen, Z.Y., Wu, W.S., Liu, C.L., Chen, T., Tian, W.Y., Li, C., 2011. Adsorption of Se(IV) onto Beishan granite. Acta Phys.-Chim. Sin. 27, 2222–2226.
Huang, B., Zhang, J.S., Hou, J.W., Chen, C., 2003. Free radical scavenging efficiency of Nano-Se in vitro. Free Radic. Biol. Med. 35, 805–813.
Huggins, F.E., Huffman, G.P., Kolker, A., Mroczkowski, S.J., Palmer, C.A., Finkelman, R.B., 2002. Combined application of XAFS spectroscopy and sequential leaching for determination of arsenic speciation in coal. Energy Fuels 16, 1167–1172.
James, F., Roos, M., 1975. A system for function minimization and analysis of the parameter errors and correlations. Comput. Phys. Commun. 10, 343–367.
Kamei, G., Ohmoto, H., 2000. The kinetics of reactions between pyrite and O_2-bearing water revealed from in situ monitoring of DO, Eh and pH in a closed system. Geochim. Cosmochim. Acta 64, 2585–2601.
Kang, M.L., Chen, F.R., Wu, S.J., Yang, Y.Q., Bruggeman, C., Charlet, L., 2011. Effect of pH on aqueous Se(IV) reduction by pyrite. Environ. Sci. Technol. 45, 2704–2710.
Kang, M.L., Ma, B., Bardelli, F., Chen, F.R., Liu, C.L., Zheng, Z., Wu, S.J., Charlet, L., 2013. Interaction of aqueous Se(IV)/Se(VI) with FeSe/$FeSe_2$: implication to Se redox process. J. Hazard. Mater. 248–249, 20–28.
Kelsall, G.H., Yin, Q., Vaughan, D.J., England, K.E.R., Brandon, N.P., 1999. Electrochemical oxidation of pyrite (FeS_2) in aqueous electrolytes. J. Electroanal. Chem. 471, 116–125.
Klaasen, C.D., 2008. Casarett and Doull's Toxicology: The Basic Science of Poisons, seventh ed. McGraw-Hill, New York, p. 1310.
Liu, A.P., Chen, X.Y., Zhang, Z.J., Jiang, Y., Shi, C.W., 2006. Selective synthesis and magnetic properties of $FeSe_2$ and $FeTe_2$ nanocrystallites obtained through a hydrothermal co-reduction route. Solid State Commun. 138, 538–541.
Liu, X., Fattahi, M., Montavon, G., Grambow, B., 2008. Selenide retention onto pyrite under reducing conditions. Radiochim. Acta 96, 473–479.
Luther, G.W., 1997. Confirmation of a sulfur-rich layer on pyrite after oxidative dissolution by Fe(III) ions around pH 2 – comment. Geochim. Cosmochim. Acta 61, 3269–3271.
Ma, B., Nie, Z., Liu, C.L., Kang, M.L., Bardelli, F., Chen, F.R., Charlet, L., 2014. Kinetics of $FeSe_2$ oxidation by ferric iron and its reactivity compared with FeS_2. Sci. China-Chem. http://dx.doi.org/10.1007/s11426-014-5126-7.
Maurizio, C., Rovezzi, M., Bardelli, F., Pais, H.G., D'Acapito, F., 2009. Setup for optimized grazing incidence x-ray absorption experiments on thin films on substrates. Rev. Sci. Instrum. 80 (6), 063904.
McGuire, M.M., Hamers, R.J., 2000. Extraction and quantitative analysis of elemental sulfur from sulfide mineral surfaces by high-performance liquid chromatography. Environ. Sci. Technol. 34, 4651–4655.
McGuire, M.M., Banfield, J.F., Hamers, R.J., 2001. Quantitative determination of elemental sulfur at the arsenopyrite surface after oxidation by ferric iron: mechanistic implications. Geochem. Trans. 2, 25–29.
Meneghini, C., Bardelli, F., Mobilio, S., 2012. ESTRA-FitEXA: a software package for EXAFS data analysis. Nucl. Instrum. Meth. Phys. Res. Sect. B-Beam Interact. Mater. Atoms. 285, 153–157.
Metz, V., Kienzler, B., Schussler, W., 2003. Geochemical evaluation of different groundwater-host rock systems for radioactive waste disposal. J. Contam. Hydrol. 61, 265–279.
Monesi, C., Meneghini, C., Bardelli, F., Benfatto, M., Mobilio, S., Manju, U., Sarma, D.D., 2005. Local structure in $LaMnO_3$ and $CaMnO_3$ perovskites: a quantitative structural refinement of mn K-edge XANES data. Phys. Rev. B 72 (17).
Moses, C.O., Herman, J.S., 1991. Pyrite oxidation at circumneutral pH. Geochim. Cosmochim. Acta 55, 471–482.
Murphy, R., Strongin, D.R., 2009. Surface reactivity of pyrite and related sulfides. Surf. Sci. Rep. 64, 1–45.
Naveau, A., Monteil-Rivera, F., Guillon, E., Dumonceau, J., 2007. Interactions of aqueous selenium(-II) and (IV) with metallic sulfide surfaces. Environ. Sci. Technol. 41, 5376–5382.
Olin, Å., Nolang, B., Osadchii, E.G., Öhman, L.O., Rosen, E., 2005. Chemical Thermodynamics 7: Chemical Thermodynamics of Selenium. Elsevier, Amsterdam.
Paschka, M.G., Dzombak, D.A., 2004. Use of dissolved sulfur species to measure pyrite dissolution in water at pH 3 and 6. Environ. Eng. Sci. 21, 411–420.
Pokrovski, G.S., Kara, S., Roux, J., 2002. Stability and solubility of arsenopyrite, FeAsS, in crystal fluids. Geochim. Cosmochim. Acta 66, 2361–2378.
Rahim, S., Milne, J., 1996. Studies on the interaction of selenite and selenium with sulphur donors. 4. Thiosulfate. Can. J. Chem.-Rev. Can. Chim. 74, 753–759.
Ravel, B., 2001. ATOMS: crystallography for the X-ray absorption spectroscopist. J. Synchrot. Radiat. 8, 314–316.
Ravel, B., Newville, M., 2005. ATHENA, ARTEMIS, HEPHAESTUS: data analysis for X-ray absorption spectroscopy using IFEFFIT. J. Synchrot. Radiat. 12, 537–541.
Rayman, M.P., 2008. Food-chain selenium and human health: emphasis on intake. Br. J. Nutr. 100, 254–268.
Ressler, T., Wong, J., Roos, J., Smith, I.L., 2000. Quantitative speciation of Mn-bearing particulates emitted from autos burning (methylcyclopentadienyl)manganese tricarbonyl-added gasolines using XANES spectroscopy. Environ. Sci. Technol. 34, 950–958.
Rimstidt, J.D., Vaughan, D.J., 2003. Pyrite oxidation: a state-of-the-art assessment of the reaction mechanism. Geochim. Cosmochim. Acta 67, 873–880.
Sasaki, K., Tsunekawa, M., Ohtsuka, T., Konno, H., 1995. Confirmation of a sulfur-rich layer on pyrite after oxidative dissolution by Fe(III) ions around pH 2. Geochim. Cosmochim. Acta 59, 3155–3158.
Savage, K.S., Tingle, T.N., O'Day, P.A., Waychunas, G.A., Bird, D.K., 2000. Arsenic speciation in pyrite and secondary weathering phases, Mother Lode Gold District, Tuolumne County, California. Appl. Geochem. 15, 1219–1244.
Schaufuss, A.G., Nesbitt, H.W., Kartio, I., Laajalehto, K., Bancroft, G.M., Szargan, R., 1998. Incipient oxidation of fractured pyrite surfaces in air. J. Electron Spectrosc. Relat. Phenom. 96, 69–82.
Scheinost, A.C., Charlet, L., 2008. Selenite reduction by mackinawite, magnetite and siderite: XAS characterization of nanosized redox products. Environ. Sci. Technol. 42, 1984–1989.
Scheinost, A.C., Kirsch, R., Banerjee, D., Fernandez-Martinez, A., Zaenker, H., Funke, H., Charlet, L., 2008. X-ray absorption and photoelectron spectroscopy investigation of selenite reduction by Fe(II)-bearing minerals. J. Contam. Hydrol. 102, 228–245.
Seby, F., Potin-Gautier, M., Giffaut, E., Borge, G., Donard, O.F.X., 2001. A critical review of thermodynamic data for selenium species at 25 °C. Chem. Geol. 171, 173–194.
Simon, G., Huang, H., Penner-Hahn, J.E., Kesler, S.E., Kao, L.S., 1999. Oxidation state of gold and arsenic in gold-bearing arsenian pyrite. Am. Miner. 84, 1071–1079.
Swartz, W.E., Wynne, K.J., Hercules, D.M., 1971. X-ray photoelectron spectroscopic investigation of group-VI-A elements. Anal. Chem. 43, 1884–1887.
Viollier, E., Inglett, P.W., Hunter, K., Roychoudhury, A.N., Van Cappellen, P., 2000. The ferrozine method revisited: Fe(II)/Fe(III) determination in natural waters. Appl. Geochem. 15, 785–790.
Webb, S.M., 2005. SIXpack: a graphical user interface for XAS analysis using IFEFFIT. Phys. Scr. T115, 1011–1014.
Weerasooriya, R., Tobschall, H.J., 2005. Pyrite-water interactions: effects of pH and pFe on surface charge. Colloid Surf. A-Physicochem. Eng. Asp. 264, 68–74.
Williamson, M.A., Rimstidt, J.D., 1993. The rate of decomposition of the ferric–thiosulfate complex in acidic aqueous-solutions. Geochim. Cosmochim. Acta 57, 3555–3561.
Williamson, M.A., Rimstidt, J.D., 1994. The kinetics and electrochemical rate-determining step of aqueous pyrite oxidation. Geochim. Cosmochim. Acta 58, 5443–5454.
Xu, Y., Schoonen, M.A.A., 1995. The stability of thiosulfate in the presence of pyrite in low-temperature aqueous-solutions. Geochim. Cosmochim. Acta 59, 4605–4622.